EFFECT OF HOT ROLLING AND INTERMITTENT ANNEALING ON THE TEXTURE EVOLUTION OF MONOTECTOID BCC ZR-NB

A Dissertation
Presented to
The Academic Faculty

by

Tanvi Dave

In Partial Fulfillment
of the Requirements for the Degree
Master of Science in the
School of Material Science and Engineering

Georgia Institute of Technology
December 2017

EFFECT OF HOT ROLLING AND INTERMITTENT ANNEALING ON THE TEXTURE EVOLUTION OF MONOTECTOID BCC ZR-NB

Approved by:

Dr. Hamid Garmestani, Advisor
School of Material Science and Engineering
Georgia Institute of Technology

Dr. Chaitanya Deo
School of Nuclear and Radiological Engineering
Georgia Institute of Technology

Dr. Preet Singh
School of Material Science and Engineering
Georgia Institute of Technology

Date Approved: December 05, 2017

ACKNOWLEDGEMENTS

It is my pleasure to take this opportunity to acknowledge my advisor, Dr. Hamid Garmestani, who has provided guidance and wisdom during my graduate studies at Georgia Tech. I am grateful for his unfailing enthusiasm and motivation throughout all stages of this research. I would also like to thank Dr. Chaitanya Deo who helped focus the direction of the research and offered valuable and constructive feedback as well as Dr. Preet Singh for his insights and discussions regarding various topics in this project. Futher, I would like to acknowledge the Department of Homeland Security's DNDO for providing the funding for this Nuclear Forensics project.

The experimental work in this research pertaining to processing and X-ray analysis was performed with help from Jacob Startt, and therefore my sincere thanks are extended to him. I would also like to recognize my lab mates, Jason Allen and Eric Hoar, for their stimulating discussions and valued input regarding texture analysis.

Finally, I am thankful for the continuous encouragement and moral support from my family. My parents, my sister, and my boyfriend have stood by me through every challenge I encountered and every victory I achieved. This thesis would not have been completed without their continuous love and support.

TABLE OF CONTENTS

LIST OF TABLES

LIST OF FIGURES

SUMMARY

Microstructural analysis of interdicted Uranium alloys may reveal information regarding their processing history which can ultimately lead to the establishment of the origin of the interdicted nuclear material. Derivation of the process parameters of these materials can provide the necessary tools to analyze the microstructural evolution of the material at each stage in the process path. Zirconium-Niobium was chosen as the surrogate material for U-Nb due to their similarities in thermodynamic behavior and presence of metastable phases. The microstructural evolution of drop-cast, β-quenched, monotectoid Zirconium-Niobium was monitored as the alloy underwent a hot-rolling and intermittent annealing process to height reductions of 10%, 20%, 30% and 40%. Samples were characterized using optical microscopy, X-ray diffraction (XRD), electron back scatter diffraction (EBSD) to investigate changes in grain size, phase, microtexture and texture. The texture of the β-phase Zr-Nb alloy is analyzed by calculating the orientation distribution functions (ODF's) and discussed in terms of the typical rolling and recrystallization texture components of BCC alloys. The rolling and recrystallization textures are well understood for BCC materials that undergo such processing over one pass however the overarching effect on final texture of a material that is repeatedly rolled and annealed has been less frequently studied. Changes in the initial texture of the Zr-18wt% Nb alloy as it undergoes each hot-rolling and annealing step leads to unconventional patterns of texture evolution as sample reduction is increased. This work aims to report and explain how such patterns may arise and how these patterns differ when comparing

texture to microtexture. Finally, this work provides the experimental texture, microtexture, and grain size data necessary for verification of an inverse process path model.

CHAPTER 1. INTRODUCTION

1.1 Motivation

In the case of illicit trafficking of nuclear materials, or a nuclear attack on the United States it is necessary to have the capabilities to intercept, collect, and analyze any nuclear weapons or debris and determine its origin in a timely fashion. Nuclear forensics aims to determine robust and predictive signatures of nuclear materials in order to determine the origin of the material. Isotopic signatures, microstructure morphology, and chemical composition all contribute to identification of the material and its origin. The data that is collected is then compared to empirical data from various databases or is computationally interpolated from existing models of tested material systems.

The incorporation of material science into nuclear forensics allows for the analysis of microstructure-processing relationships of a material in order to determine the material's processing history. For the processing of nuclear fuels or structural components, suitable processing steps for investigation would include casting, hot or cold rolling, annealing, homogenization, or quenching. Such processing steps of actinide alloys can introduce discriminating microstructural elements such as phase or morphological changes. These changes can act as signatures that can be characterized at each step in the processing path.

In the following work, we attempt to take the first step towards this goal of predicting a materials processing history by understanding the structure-processing relationship of an actinide alloy as it undergoes thermo-mechanical processing. The chosen system for this study was a zirconium niobium which is commonly used in the nuclear industry and a

suitable surrogate for uranium-niobium which significantly populates the US nuclear stockpile. Arc-melted Zr-18Nb was processed by hot rolling to 10%, 20%, 30% and 40% reductions for the purpose of capturing the microstructural evolution of this material. This evolution was measured by collecting texture data using X-ray diffraction and micro-texture data from electron back scattered diffraction. Texture data provides information regarding the materials anisotropy and phase composition which can change due to processing and can be portrayed using pole figures and orientation distribution functions (ODF).

An inverse process modeling methodology would input a materials microstructural data such as texture, secondary phases, and grain size to reverse engineer the fabrication process based on fixed parameters such as temperature and strain rate. The microstructure from each step in a processing path would generate a point in a microstructural hull which is a 3D space that encompasses the entire microstructure-process design space. Following a microstructural evolution would be equivalent to following a streamline of points in the microstructure hull which would depict the path for a single type of processing such as hot rolling. Varying parameters of processing would cause a shift in the streamline, and varying a process altogether would generate and completely new streamline. From this model, an optimal processing path can be determined from a given microstructure and therefore provide predictive capabilities. The single microstructure could then be plotted in the hull and the processing which led to this microstructure could then be narrowed down to a handful of paths from which a nuclear forensic analyst could narrow down those most likely based on statistical considerations.

CHAPTER 2. BACKGROUND

In their pure form Group IV-B transition elements such as Ti, Zr, and Hf and actinide elements such as U and Pu exhibit a non-cubic phase which is stable at low temperatures, and a body-centered cubic (BCC) phase stable at elevated temperatures. Alloying additions (e.g. Nb, V, Fe, MO, Mn, and Cr) can help stabilize the BCC phase (often referred to as the beta phase) at lower temperatures. The alloy phase diagrams often exhibit eutectoid or monotectoid transformations between stabilized beta phase and the non-cubic phase(s) [1]. These transformations depend on cooling rates from the melt as well as processing conditions. While many investigations of β-Ti alloys and their structure-processing relationships have been conducted, there is little information available regarding highly alloyed β-Zr alloys. The effect of processing on the phase structure of alloys such as U-Nb and Zr-Nb is of particular interest due to their applications in the nuclear industry.

2.1 Zr-Nb System

Zirconium niobium alloys are used in various nuclear structural applications. Commonly it is used in fuel cladding material due it its corrosion resistance and high temperature performance [2]. Irradiation stability and prevention of creep are also among the qualities of this alloy that make it attractive for nuclear reactor structural materials [3]. The Zr-Nb alloy system has also long been associated with advancements in the biomedical implant industry. With low magnetic susceptibility, Zr-16%Nb is a suitable candidate for biomedical implants as it reduces MRI imaging artifacts which occlude the visibility of physiology near the implantation sites [4]. The biocompatibility has also been widely studied, and it is indicated that Zr-22%Nb is shows high corrosion resistance. A wide range

of Zr-Nb alloys also show low cytotoxicity making them promising for biomedical applications [5].

The properties of zirconium niobium are dictated largely by the composition of the alloy. For the purpose of comparison, we discuss the properties and microstructural characteristics of Zr-Nb by separating the system into three parts: Zr-rich alloys, intermediate composition Zr-Nb, and Nb-rich alloys. The phase diagram of Zr-Nb in Figure 1 can be used to follow along with the phase transformations discussed in the next sections

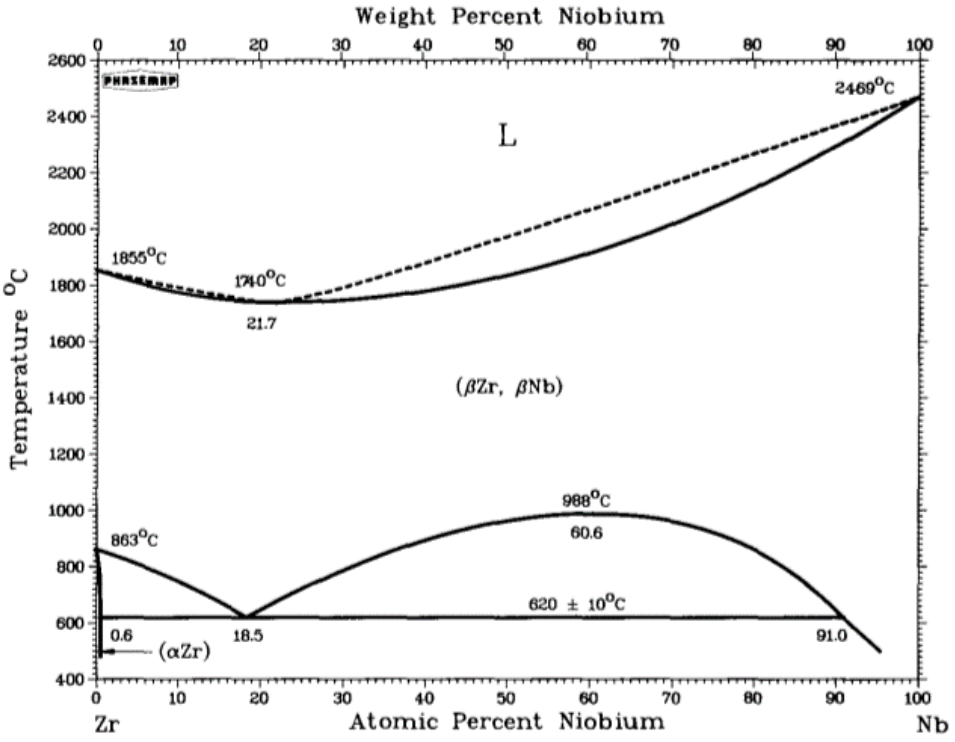

Figure 1: Phase diagram of the Zr-Nb system [6]

2.1.1 Zirconium-Rich Alloys

The phases present in the Zr-Nb system at low Nb concentrations include β-Zr at high temperatures which when quenched can transform almost entirely into the metastable martensitic α' phase [6]. Ageing of these alloys below the monotectoid temperature at 620°C can lead to a separation of the α-Zr and β-Nb phases which in turn yield different properties. Zirconium-rich Zr-Nb alloys are commonly used in the structural components of nuclear reactors due to their mechanical strength and low neutron absorption. Low niobium concentration is also attributed to increased corrosion resistance which allows for the use of Zr-2.5% Nb alloy in high pressure water reactors [7, 8].

2.1.2 Intermediate Zr-Nb Alloys

With an increase in the Nb content the phases that make up the alloys begin to change. When the high temperature beta is quenched the martensitic α' phase no longer forms beyond 7.5% Nb composition, and the β-phase is retained without the formation of the hcp α-phase. Additionally, this metastable β can decompose to form a hexagonal non-equilibrium ω-phase. Upon quenching from the β-phase to room temperature, the formation of ω is athermal and reversible. From this transformation, an increase in embrittlement and a superconducting properties were observed [9]. Isothermal ω is formed by ageing below 500°C. Strain-induced and high pressure-induced ω- phases have also been studied [6, 10]. The metastable ω-phase has been of key interest in many zirconium and titanium alloys which have been quenched from a high temperature β phase. The formation of the isothermal ω phase has been shown to also serve as a nucleation site for α

precipitation upon ageing in both Titanium and Zirconium alloys [10, 11]. The α-precipitates form along the grain boundaries and in the bulk BCC matrix.

A key transformation in belonging to this composition range is the monotectoid reaction. Slow cooling from the high temperature solid β-phase at approximately 18.5wt% Nb results in the formation of a Zr-rich α-phase and a Nb-rich β-phase.

$$\beta_1 \leftrightarrow \alpha + \beta_2$$

The two β-phases are separated by a miscibility gap in the Zr-Nb systems which results in two phases with the same crystal structure but different compositions [6].

2.1.3 Niobium-Rich Alloys

In the niobium-rich region of the Zr-Nb system beyond the monotectoid composition, there is a miscibility gap that separates the homogenized high temperature β-phase into β-Zr and β-Nb. This high temperature reaction forms a lamellar structure. Below the monotectoid temperature, alpha precipitates at the grain boundaries and a niobium rich beta phase is formed with a cellular morphology [12]. The ω-phase does not form by room temperature quenched beyond 30% Nb content and for this reason alpha precipitation is more likely to form along grain boundaries and dislocations within the matrix upon ageing quenched Nb-rich alloys.

2.1.4 Zr-Nb Deformation Modes

Plastic deformation in metals occurs by slip or twinning, and in the case of BCC metals, slip always occurs on the close packed <111> direction. The slip planes may vary

with material but are commonly the {110}, {112}, and {123} planes [13, 14]. Some studies on Zr-Nb metastable β phase have observed twinning in the {332}<113> system due to the instability of β to ω (hcp) decomposition [15]. Additionally twinning in the {112}<111> orientation was observed after increased solution hardening from deformation in the sample which prevents {112}<111> slip. Such deformation modes were observed in Zr-Nb alloys as well as Titanium alloys due to their similarities as metastable beta phase alloys with athermal ω-phases.

2.2 Surrogate Material for Uranium-Niobium

Uranium-6wt% Niobium is heavily populated in the US nuclear stockpile due to its corrosion resistance and mechanical workability. Much of the current interest in the alloy is focused on the aging of the alloy and the resulting effects on the corrosion and mechanical properties [16]. The Zirconium 18 wt% Niobium alloy was chosen as a surrogate for the U-6Nb. Similar to Zr-Nb, the U-Nb alloy (phase diagram shown in Figure 2) undergoes the monotectoid reaction at U-6wt%Nb from a high temperature body BCC phase and upon quenching it forms metastable phases. According to the U-Nb phase diagram, at 645°C the BCC γ-phase decomposes into orthorhombic U-rich α-phase and the Nb-rich γ-phase at equilibrium [17]. However in practice upon rapid cooling, the high temperature γ-phase initially undergoes a lattice distortion to form an ordered tetragonal γ°-phase, and before the formation of the α-Uranium phase, an α'-martensite is formed followed by a monoclinic distortion which forms the α''-martensite phase. The U-6wt%Nb alloy has been also studied for its shape memory effects of its γ → α'' transformation [18]. Though the nature of the metastable phases of monotectoid Zr-Nb and U-Nb differ, the

simpler Zr-Nb system was chosen to facilitate the ease of experimentation and generate a reliable model which could then be applied to the U-Nb system.

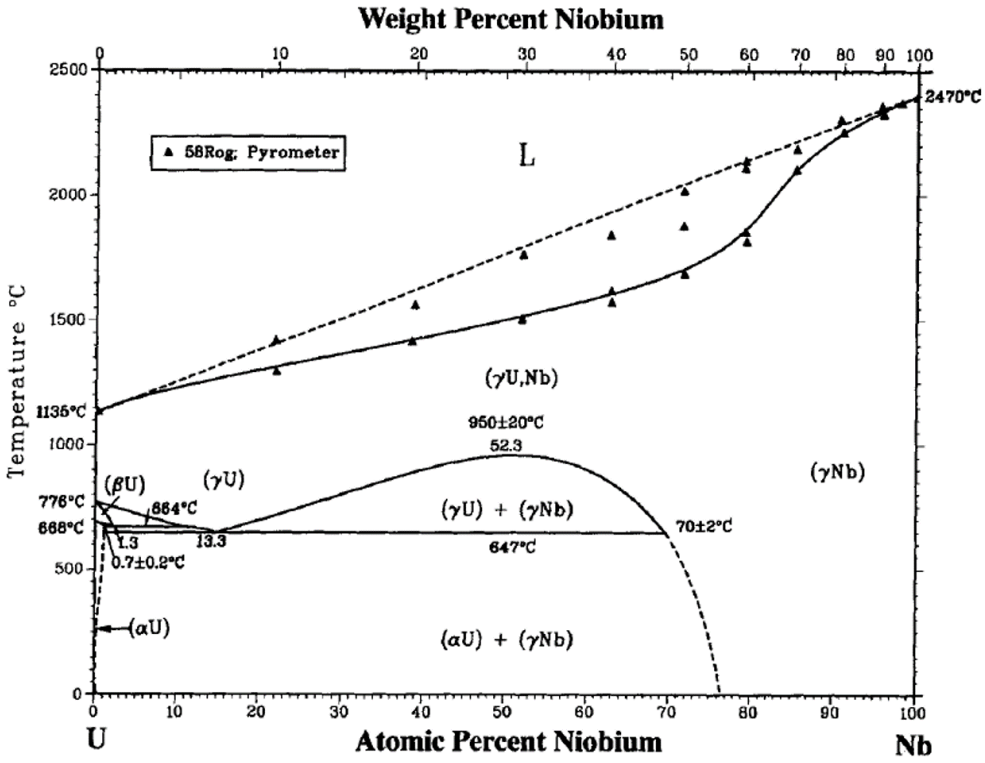

Figure 2: Phase diagram of the U-Nb system [17]

2.3 Zr-Nb in this work

Though Zr-Nb alloys have a wide range of applications based on their composition, ageing, and mechanical processing, this report will focus on the monotectoid Zr-Nb alloy. Beta-quenched monotectoid Zr-Nb largely retains its BCC phase at room temperature. In this work, the microstructural evolution of this alloy is investigated as it undergoes hot-rolling. The characterization of morphological features which as serve as microstructural signatures is of particular interest in this experimental study. Anything from pores, twins,

changes in grain shape/size, phase change, and texture change can be considered a signature for input into an inverse model. The as-received samples used in this study were drop-cast with a composition of 18.2 % Nb and beta-quenched. At this composition, there are 3 different phases one can expect to see during processing. These include the BCC β-phase, an HCP ω-phase which forms athermally, and the HCP α-phase. If the β -quenched alloy is aged, the homogenous solution β phase can decompose into niobium rich β and zirconium rich α completing the monotectoid reaction [6]. The athermal omega can also be expected to form at the nanoscale upon quenching. A schematic of the α, β, and ω unit cells are shown in Figure 3.

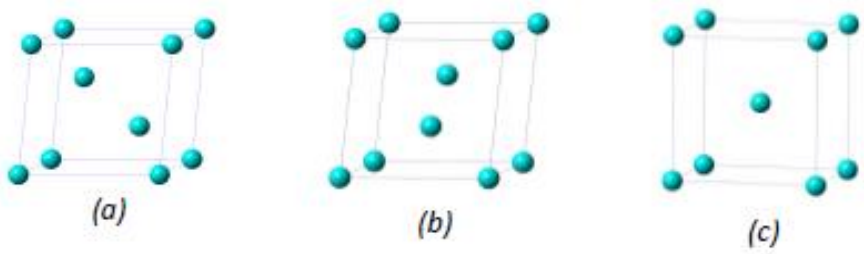

Figure 3: Unit cells for a) HCP α-phase b) HCP ω-phase c) BCC β-phase

The study of the microstructural evolution through texture data may allow one to predict possible processing paths from a given final microstructure. With an understanding of the processing capabilities of various manufacturers, the origin of a material can ultimately be pin-pointed. Such a tool if applied to nuclear materials would facilitate in determining the provenance of interdicted nuclear weapons materials.

2.4 Texture

Most metals are polycrystalline materials whose properties depend on the directionality of their crystals. The statistical distribution of crystallite orientation within

a polycrystalline material is commonly referred to as texture. A material is said to be "textured" if a large fraction of the crystallites are oriented in a particular direction. In contrast, if the crystallites in the material are show no preference in orientation, then the material is "textureless" or randomly oriented. The orientation of crystallites within a polycrystalline material are not necessarily constant. Texture of a material can change with thermomechanical processing.

The orientation of a crystallite is can be represented by its rotation from a coordinate system defined by the sample material. A common method of describing the rotation in Bunge notation is using Euler angles: φ_1, ϕ, and φ_2. If the sample material's orientation is represented by a normal Cartesian coordinate system with x, y and z coordinates, then the orientation of the crystallites is described by the following [19]:

1. φ_1: rotation about the Z axis of the sample coordinate system (Z1)
2. ϕ: rotation about the new X axis now written as X1 after the first rotation
3. φ_2: rotation about the new Z axis now written as Z2 after the second rotation

Figure 4 illustrates the rotation of the individual crystallite with respect to the sample. The rotations must be carried out in the above order to avoid inaccurately representing the crystal orientation. With each Euler angle defined, a 3D Euler space can be conceptualized which would contain every possible orientation possible for any crystallite. These orientations can also be referred to as texture components using the miller notation

{hkl}<uvw>, where {hkl} is a plane normal to the normal direction (ND) and <uvw> is a direction parallel to the rolling direction (RD).

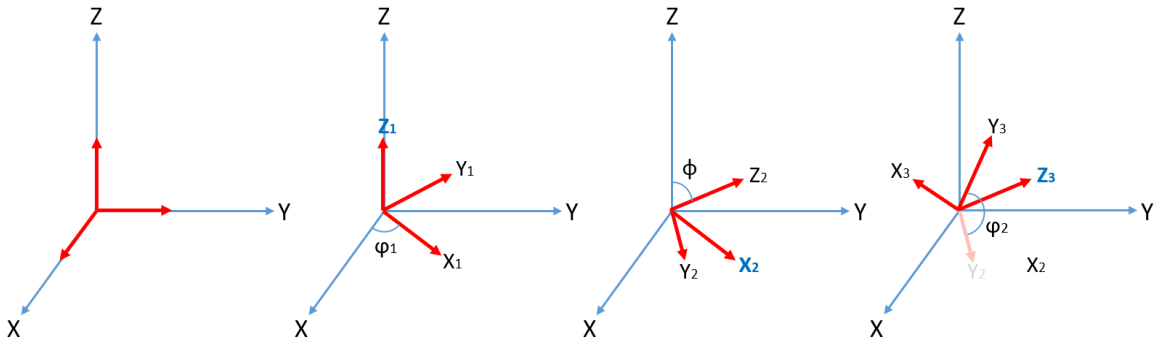

Figure 4: Illustration of Euler angle rotation procedure to define crystal orientation with respect to sample orientation.

In order to represent the texture of a material, it is a well-established practice to use pole figures. Pole figures can describe how a certain crystal orientation is distributed with respect to the sample. If one imagines a hollow sphere with a single crystallite at its center, a certain <hkl> direction for that crystallite will pierce the sphere at a specific location. If a stereographic projection of the sphere is made, then the location at which the <hkl> direction pierced the sphere will represent a "pole" for that crystallite in the stereographic projection. In a polycrystalline material, if the poles are randomly distributed within the stereographic projection, then the material has random texture [20]. If the poles tend to cluster in certain locations on the stereographic projection, then the material is textured. An example of a pole figure before and after rolling is shown in Figure 5: Schematic showing the transformation from random textured pole figure **to highly textured pole figure due to rolling.**

.

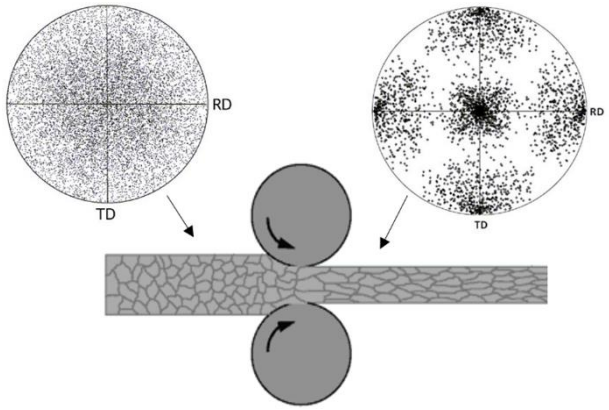

Figure 5: Schematic showing the transformation from random textured pole figure to highly textured pole figure due to rolling.

Although the pole figure provides texture information for a specific crystallographic plane, it is necessary to quantify the distribution of all the crystallographic orientations in a sample for a complete understanding of a material's texture. A more complete method of portraying texture is to plot each crystallite as a point in the 3D Euler space whose coordinates are the three Euler angles. The distribution of these points in the Euler space is called the orientation distribution function (ODF) [21]. Like in the pole figure, clustering in the 3D Euler space is representative of texture and a random distribution of these points is the lack there of. If the clustering of points occurs along a linear path in the ODF, we can label this as a fiber in the ODF.

Bunge used spherical harmonics in order to calculate the ODF [21]. The orientation of a single crystallite is denoted as g where g = g(ϕ_1, φ, ϕ_2). The ODF is expressed below:

$$f(\varphi_1, \phi, \varphi_2) = \sum_{l=0}^{\infty} \sum_{m=-l}^{+l} \sum_{n=-l}^{+l} c_l^{mn} T_l^{mn}(g)$$

2.4.1 X-Ray Diffraction

X-ray diffraction is a versatile tool used to determine phases, unit cell lattice parameters, and crystal orientations and structure. X-ray diffraction occurs when x-rays are incident upon a crystal lattice whose atomic spacing is on the order of the wavelength of the x-rays. The utility of XRD in crystallography is dependent on the Bragg condition which states that constructive interference between two reflected x-ray beams will occur when the distance they travel differs by a whole number multiple of the wavelength of the x-ray. This diffraction is illustrated in Figure 6 and can be simply stated mathematically by the following Bragg's Law:

$$n\lambda = 2d \sin\theta$$

where

$n = any\ integer\ (1, 2, 3, etc\ \ldots)$

$\lambda = wavelength$

$d = atomic\ spacing\ or\ interplanar\ spacing$

$\theta = angle\ at\ which\ the\ wave\ is\ incident\ on\ the\ sample$

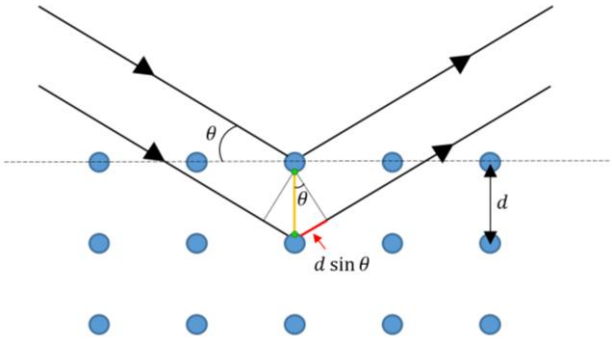

Figure 6: Illustration of incident and reflected x-ray beams off a crystal surface demonstrating the condition for constructive interference

By controlling the incident angle and knowing the wavelength of the x-ray, one can use Bragg's Law to calculate the lattice spacing. In a periodic crystal lattice, the d-spacing between different planes at different orientations can be measured by changing the θ angle. In a XRD experiment, the sample is fixed onto a goniometer which is used to position the sample so that is hit at range of angles by the incident beam and the diffraction pattern is collected. A peak intensity occurs when constructive interference of reflected waves occur. The 2θ angle at which the high intensity peaks occur represent planes separated by a particular d-spacing. By correlating the d-spacing to particular planes, a series of pole figures can be generated to describe texture. Finally, multiple pole figures can be used to calculate an ODF.

2.4.2 Electron Backscatter Diffraction

Electron back scatter diffraction is a method of collecting crystal orientation data and identifying phase on a local region of a sample surface from within a scanning electron microscope (SEM). In the typical set-up for EBSD data collection, the sample is tilted to 70° relative to the SEM electron beam and faces the vertically oriented EBSD detector

which contains a phosphor screen. When the incident beam hits the sample some electrons are backscattered and projected onto a phosphor screen to generate a series of bands called a Kikuchi pattern. The Kikuchi pattern is a representation of the crystal planes of a specific point on the sample that is hit by the incident electron beam. The pattern is analyzed by the computer and compared to the database of a Kikuchi patterns for a specific material and phase to determine the crystal orientation of the small point on the sample. High speed EBSD data acquisition allows for one to collect orientation data of a large area of the sample. An EBSD scan can discern individual grains, twins, secondary phases and even dislocations in a material [20]. In this work the Zr-Nb samples are characterized with EBSD using a beam voltage of 20kV. A schematic of the experimental set-up of the EBSD is shown in Figure 7a. Figure 7: a) The set-up for EBSD showing the sample in brown and the backscattered electrons projected onto the EBSD detector to form a Kikuchi pattern. [20] b) Example of an EBSD scan showing crystallite orientation from grain to grain. b shows an example of an EBSD inverse pole figure map in which the colors represent the

particular crystal orientation. Figure 7b also illustrates how individual crystallites can be represented as rotations of the sample coordinate system.

EBSD performs a scan and collects texture data for a local region on the surface of a sample. The orientation data attained from EBSD is referred to as micro-texture due to the localized region from which the data is obtained and the shallow penetration into the surface of the sample. However, EBSD data provides a physical representation of the distribution of orientation in a sample. The EBSD image mirrors an optical microscopy image in that the change in orientation highlights individual grains or phases in the EBSD scan.

2.5 Rolling and Recrystallization Textures for BCC Materials

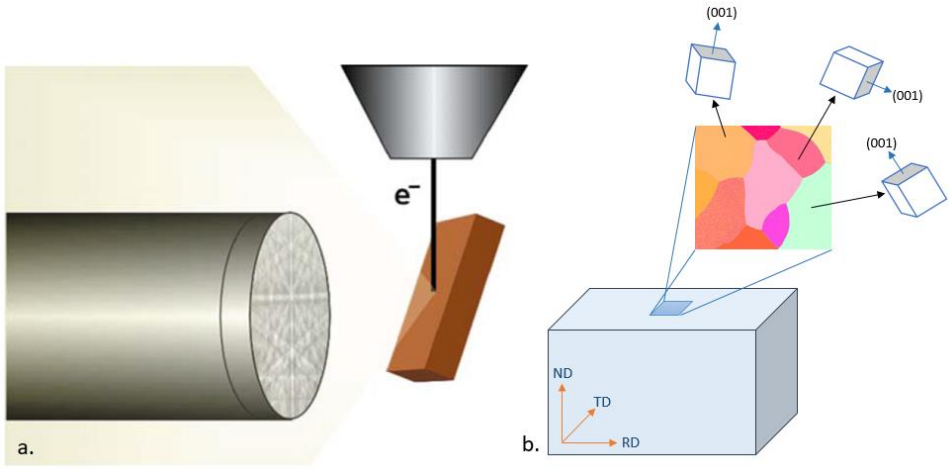

Figure 7: a) The set-up for EBSD showing the sample in brown and the backscattered electrons projected onto the EBSD detector to form a Kikuchi pattern. [20] b) Example of an EBSD scan showing crystallite orientation from grain to grain.

Rolling texture is consistent among most BCC metals and alloys but slight differences in texture is known to arise due to composition and initial microstructure [22]. Rolling BCC texture is best characterized by fibers in the ODF. A texture fiber is defined as a string of high intensity regions in the Euler space containing multiple texture components. Typically in BCC metals, rolling texture components are concentrated within two main fibers: the α-fiber and γ-fiber. The α-fiber contains all texture components where <110> is parallel to the rolling direction (RD), and the γ-fiber contains all texture components where <111> is parallel to the normal direction (ND) [13]. A less commonly discussed fiber in BCC metals includes the θ-fiber which contains the texture components where <001> is parallel to ND [23]. Table 1 summarizes the various fibers observed in BCC materials.

Table 1: Typical fibers observed in rolled and recrystallized BCC metals and alloys along with their fiber axes and individual texture components [23]

Fiber	Fiber Axis	Texture Components or Orientations
α - fiber	<110> // RD	{001}<110>, {112}<110>
γ - fiber	<111> // ND	{111}<110>, {111},<112>
θ - fiber	<001> // ND	{001}<100>, {001}<110>
η - fiber	<001> // RD	{001}<100>, {011}<100>
ε - fiber	<011> // TD	{001}<110>, {112}<111>, {4 4 11}<11 11 8>, {111}<112>, {11 11 8}<4 4 11>, {011}<100>

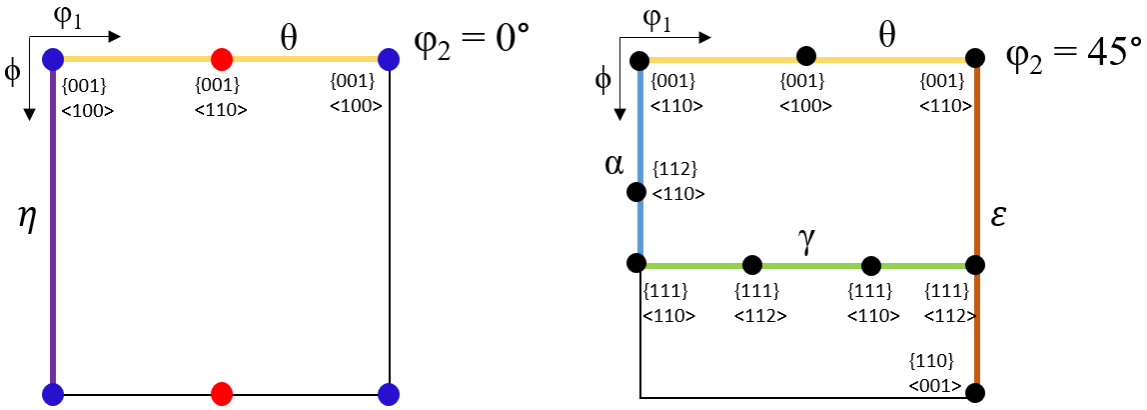

Figure 8: ODF sections $\varphi_2 = 0°$ and $\varphi_2 = 45°$ showing common texture components and fibers formed during rolling and recrystallization of BCC metals and alloys.

A schematic of the BCC texture components represented in the ODF is shown in Figure 8 where the $\varphi_2 = 0°$ section is shown to the left and the $\varphi_2 = 45°$ section is on the right. Hot rolling is known to create inhomogeneous textures through a materials thickness. The surface may exhibit shear components such as Goss {011}<001>, and the center will

exhibit cold rolling textures such as a strong α-fiber components especially {001}<110> and a weak γ-fiber [22-25]. Some highly corrosion resistant ferritic stainless steels, most Si-steels, and pure BCC metals (Ta, Nb, or Mo) tend to reveal cold-rolling textures in the central layers after hot rolling [23, 26]. Cold rolling tends to sharpen and increase the intensity of the material's texture and therefore shows a strong α-fiber namely the {001}<110> and {112}<110> components and a relatively weaker γ-fiber [27]. In addition to the texture fibers, rolling can introduce rotated cube texture components, {001}<110>.

Recrystallization occurs in three steps during the annealing process: 1) recovery, 2) nucleation, and 3) grain growth. During recovery, there is no change in microstructure, rather the stored energy within the deformed microstructure is reduced when the material is annealed to low temperatures. At higher temperatures, recrystallization takes place by the nucleation of new strain free grains. This recrystallization stage is described by two theories: Orientation Nucleation which states that texture is dependent on the growing nuclei of favourable orientations and Growth Selection which states that the competition among differently oriented nuclei determines the final texture. Both of these theories play some role in the final grain growth stage. This stage is driven by high misorientations between the nuclei and matrix meaning that high angle grain boundaries will have higher mobility and allow for faster grain growth [28, 29]. In the context of BCC texture specifically in deep drawn steels and alloyed steels, annealing rolled materials will generally begin to randomize texture if the previous deformation was low and lead to the formation of Goss and other η components at higher deformations. With even higher deformation, a strong γ-fiber is formed and the η-fiber components decrease in intensity upon annealing [22]. Most works report a strengthening of the γ-fiber and a weakening of

the α-fiber after annealing [22, 24, 29]. The emergence of Goss, cube and rotated cube components are also discussed as evidence of recrystallization.

CHAPTER 3. EXPERIMENTAL PROCEDURE

3.1 Sample Manufacturing/Procurement

The preparation of the alloy was carried out by AMES Laboratory. The process involved arc-melting buttons starting with greater than 99.8% purity Zirconium and Niobium. Zr-81.5 Nb18.27 (at%) buttons were triple arc-melted on a water cooled copper hearth in argon atmosphere. Multiple buttons were stacked and melted together and drop-cast into a water cooled copper mold to cast a rod approximately 18mm in diameter. From the rod, one 16mm sample was cut with the TechCut5TM Precision High Speed Saw at 2100RPM and 0.25 in/min feed rate. The sample used in this experiment had a large average grain size of approximately 100 μm. Such a small sample size would have resulted in variability in the texture data from sample to sample. To avoid inaccurate comparisons of texture from multiple samples, the same sample was used throughout processing.

3.2 Hot Rolling and Heat Treatment

The samples were heat treated to 1000˚C for 5 minutes between rolling intervals in the MTI Corp GSL-1700s60 high temperature vacuum/gas furnace. After heating, the sample was quickly carried to the General Electric Motors 1960 rolling mill where it was rolled at 1% increments until approximately 10% 20%, 30%, and 40% reduction stages were reached. In between each 1% increment the sample was brought back to 1000°C for 5 minutes to ensure hot-rolling. After the final reduction was reached the sample was then heated again to 1000˚C for 5 minutes and promptly quenched in water. The true sample reduction at each stage is given in

Table 2. Because of the intermittent annealing between hot-rolling steps and subsequent annealing and quenching after the hot-rolling, each processing step will be referred to as e.g. 10% HR though there is an annealing step after each reduction stage in this study.

Table 2: True height reductions of Zr-Nb sample upon hot-rolling

	As-received	**10% HR**	**20% HR**	**30% HR**	**40% HR**
True Height Reduction	0%	9.83%	19.78%	30.10%	40.11%

3.3 Metallographic Sample Preparation

Each of the characterization methods in this project required different levels of sample preparation. Table 3 shows the complete nine steps of grinding and polishing for EBSD and SEM analysis, however the rest of characterization methods required only partial completion of the procedure. All of the sample preparation was conducted on the MetPrep 4TM from Allied High Tech Products inc. Initial preparation of the samples involved seven steps outlined by the MetPrep4TM auto-polisher. However steps 2 and 8 were added upon experimenting with polishing techniques.

For XRD analysis, the samples were polished to Step 5 from Table 3. Previous experiments showed that polishing until this step achieved the highest quality scans when compared to samples which were polished further. Step 2 was added to the original procedure to thorough mechanical polishing at coarser steps.

Optical microscopy of these samples polished using the original procedure would reveal smearing and residue of colloidal silica on the sample surface and occlude the underlying microstructure. Step 8 was then introduced which significantly improved the quality of optical microscopy images by etching the surface to produce contrast through oxidation. In this step, 0.04 μm colloidal silica is combined with 30% H2O2 at a 5:1 ratio by volume. With further variation of the polishing method, it was found that periodically washing the H2O2 + 0.04 μm colloidal silica polishing pad with water produced the cleanest samples for both optical and EBSD characterization.

For EBSD and SEM analysis, the sample was polished all the way through Step 9. After etching in Step 8 the sample had a highly uneven and oxidized surface from grain to grain whereas a completely flat surface is required for EBSD. Step 9 which involved polishing with only 0.04 micron colloidal silica for an additional 20 minutes removed the oxidized surface and flattened the surface. Increased height reduction in the samples introduced deformation and hardened the sample and therefore it required more polishing time in order to fully achieve a suitable surface for EBSD analysis.

Table 3: Metallographic Prep Procedure for Zr-Nb characterization

Step	1	2	3	4	5	6	7	8	9
Abrasive (P-Grade)	320	400	600	800	1200	3μm	1μm	0.04μm + 30% H_2O_2 (5:1 ratio)	0.04μm
Type	SiC	SiC	SiC	SiC	SiC	Polycrystalline Diamond	Polycrystalline Diamond	Silica	Silica
Carrier	Abrasive discs	Abrasive Discs	Abrasive Discs	Abrasive Discs	Abrasive Discs	Glycol suspension	Glycol suspension	Colloidal suspension	Colloidal suspension
Polishing Cloth	-	-	-	-	-	White Label	White Label	Final A	Final A
Coolant	Water	Water	Water	Water	Water	GreenLube	GreenLube	Water*	Water*
Platen Speed (RPM)/ Direction	300/ Comp	300/ Comp	300/ Comp	300/ Comp	150/ Comp	150/Comp	150/Comp	150/Comp	150/Comp
Sample Speed (RPM)	150	150	150	150	150	150	150	150	150
Force (lbF/N)	6/26	6/26	6/26	6/26	6/26	6/26	4/17	4/17	4/17
Time (min)	1-2	1	2	1	5	5	5	5	20-40**

CHAPTER 4. CHARACTERIZATION RESULTS

4.1 Optical Microscopy and α-Phase Precipitation

Optical microscopy of the as-received sample revealed homogeneous distribution of equiaxed grains with a fair amount of sub-grain morphology present in a majority of the grains. The morphology of the grains changed distinctly with increasing sample reduction and annealing as shown in Figure 9. Though the grains remained fairly equiaxed, the interior of the grains show less uniformity with increased reduction. The grain size was measured for each stage in the processing using the procedure outlined by the ASTM grain counting method [30] and the grain size is reported in

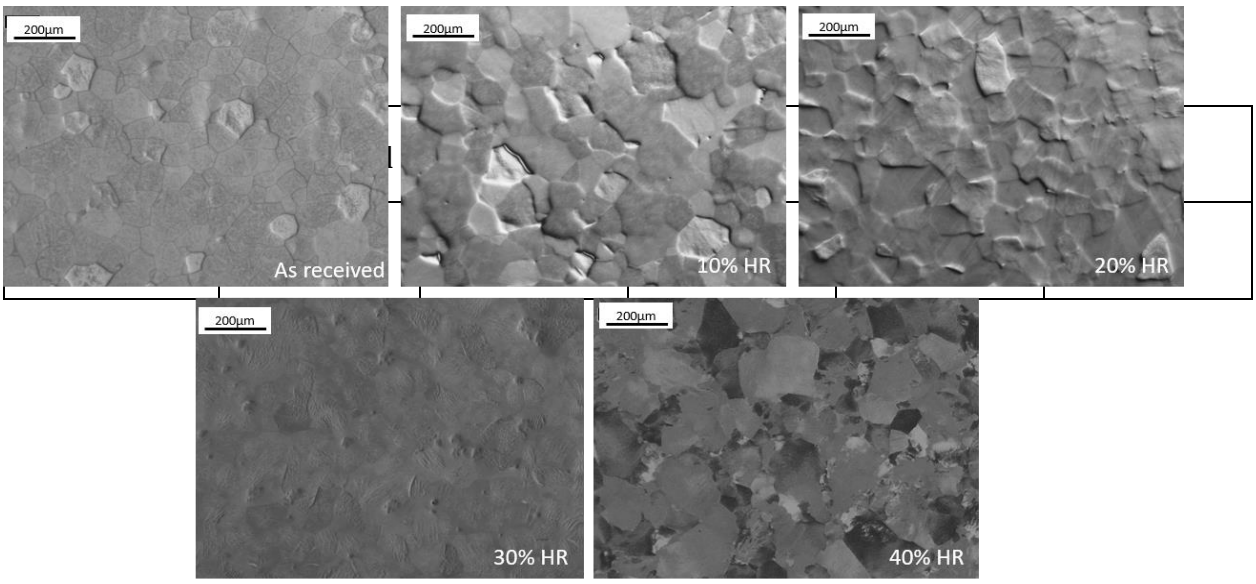

Figure 9: Optical Images of the Zr-Nb sample at each stage in the processing path.

Table 4. The grains/mm^2 decreases steadily with increased deformation. In other words the grain size increases overall as the processing path progresses. One factor that may have inhibited the growth rate of the grains would be precipitation of the α-phase at

grain boundaries which occurred after the 10% hot-rolling (HR) process. This may have caused grain boundary pinning and restricted the growth of the grains.

Table 4: Grains/mm^2 at each stage in the processing path

	As-received	**10% HR**	**20% HR**	**30% HR**	**40% HR**
Grains /mm^2	157. 76	124.19	121.99	118.13	113.96

Optical Microscopy and SEM revealed the precipitation of grain boundary and intragranular α-phase precipitates. The intergranular precipitates were both circular and oblong. If oblong they had a length ranging from 1 to 3 μm and width of 0.5-0.75 μm on average. The circular precipitates were typically 0.5-0.75 μm in diameter. The grain boundary precipitates had the same widths of intragranular precipitates but were often longer in length, some as long as 25 μm. The size and distribution of the α-phase did not

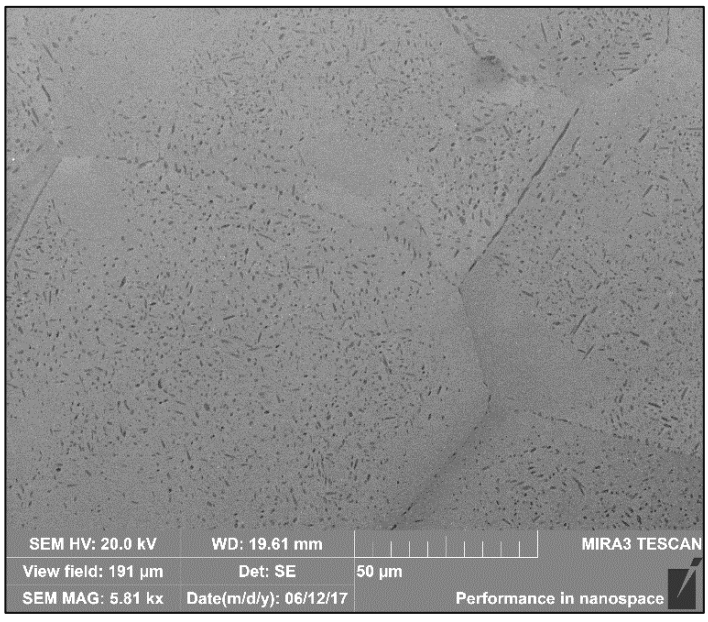

Figure 10: SEM image of α-phase precipitation in β matrix in the 10% HR sample.

change significantly through subsequent rolling procedures. The distribution of the α-phase precipitates was largely homogeneous however there were an even distribution of precipitate free pockets many located at or near grain boundaries as seen in Figure 10: SEM image of α-phase precipitation in β matrix in the 10% HR sample..

The precipitates were confirmed α-phase by EBSD analysis and X-ray diffraction results. Figure 11a shows an EBSD scan taken at a triple point in the 10% HR sample. The colors represent the orientation specified by the inverse pole figures in Figure 11d. Also shown is an image quality map (Figure 11b) and a phase map (Figure 11c).

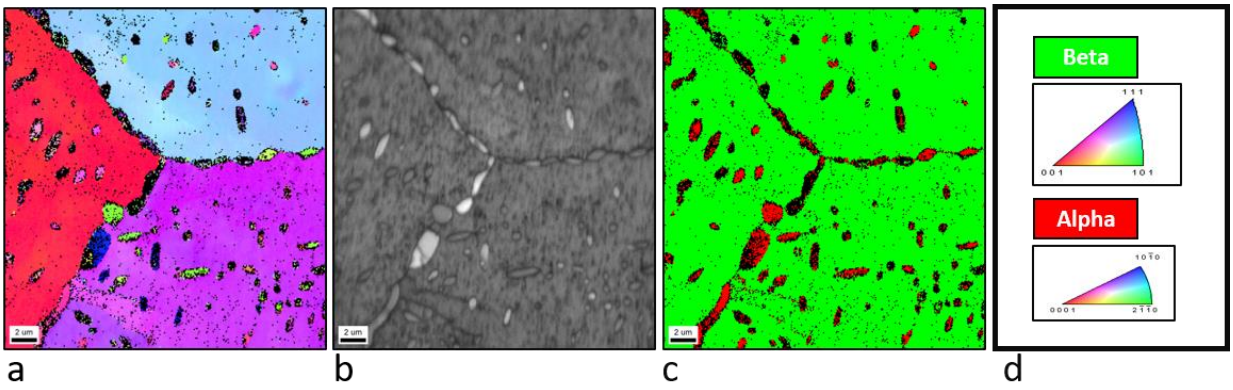

Figure 11: EBSD scan of a triple point in the 10% HR sample showing a) the inverse pole figure (IPF) map b) image quality map, c) phase map d) phase map key and IPF key for both α- and β-phases.

4.2 XRD Results

The XRD pattern for both the as-received and 40% HR samples are shown in Figure 12 and Figure 13 respectively. The as-received pattern shows primarily peaks belonging to the β-phase. It contains a minor peak for the (01-10) α-phase plane however the evidence is minor and therefore the as-received sample is almost entirely in the β-phase. The 40% HR sample contains the high intensity β peaks however the α peaks have noticeably

increased in intensity and therefore both phases are present in the sample with a majority of the β-phase. The peaks were identified by matching the observed peaks locations and intensities with simulated XRD peaks based on known Zr-Nb structures. This is due to the XRD peak data on monotectoid composition Zr-Nb in the database. All peaks observed in the XRD pattern are able to be identified, therefore we can be sure to know if other phases or contaminants are present. Due to the overlap of some α and β peaks, β-phase texture

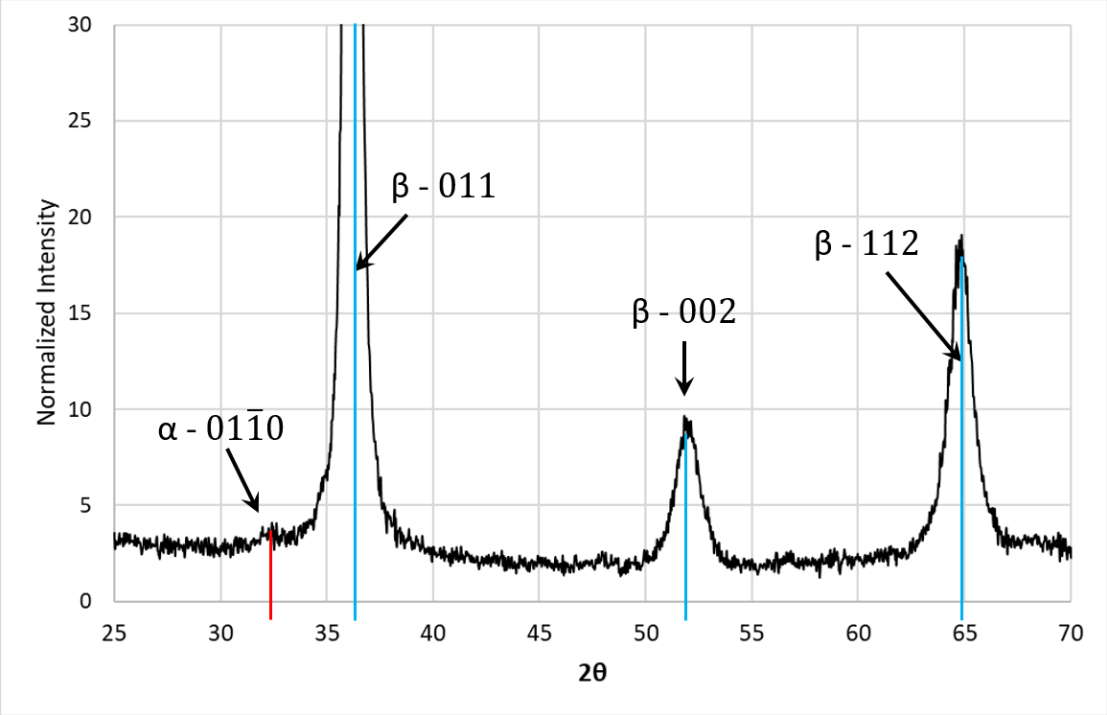

Figure 12: XRD pattern for the As-received sample.

analysis was limited to the (002), (112), (123), and (222) peaks. X-ray texture analysis is not able to be performed on the α-phase at this moment due to the low peak intensities of the α-phase and due to peak overlap of α peaks with K-β and WL-α peaks. The K-β and WL-α peaks were unable to be filtered since the MRD was not equipped with a monochromator.

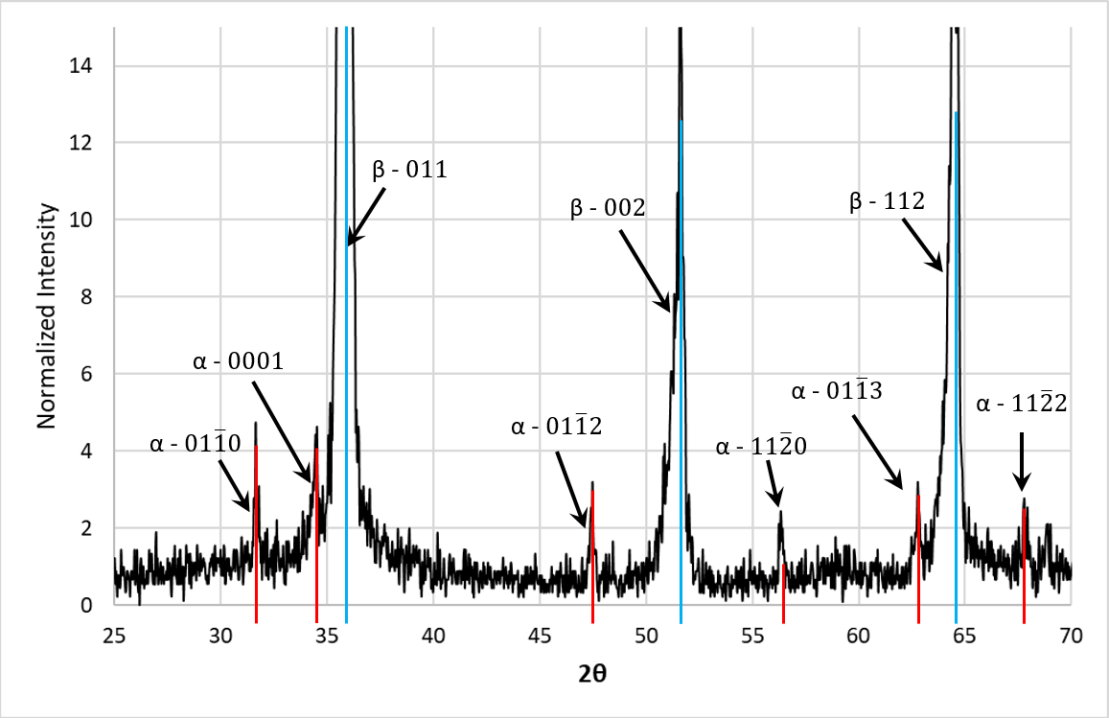

Figure 13: XRD pattern for the 40% HR sample.

4.3 EBSD Results

The EBSD scans in Figure 14 show the evolution of the microtexture at each stage in the processing path. The scans were taken on the normal surface with the rolling direction pointing downwards. The scans were taken at 20kV with a 2 μm step size. The as-cast sample shows equiaxed grains with uniform orientation within each of the grains. With increased reduction to the sample, deformation can be identified through the gradient of orientations introduced into individual grains. Deformation becomes increasingly apparent as reduction increases. Samples with 30% and 40% reduction were greatly deformed which in turn negatively affected the quality of the EBSD scan. The data for these scans were cleaned by "grain dilation" using OIM Analysis software. Though the α-phase was

present in the grains of each of the rolled samples, the size of the precipitates was small enough to not greatly affect the quality of the β only scan. Due to the small size of the α-precipitates, the α-phase texture data was not able to be captured over a large EBSD scan, and therefore the β to α transformation texture is not further investigated in this work.

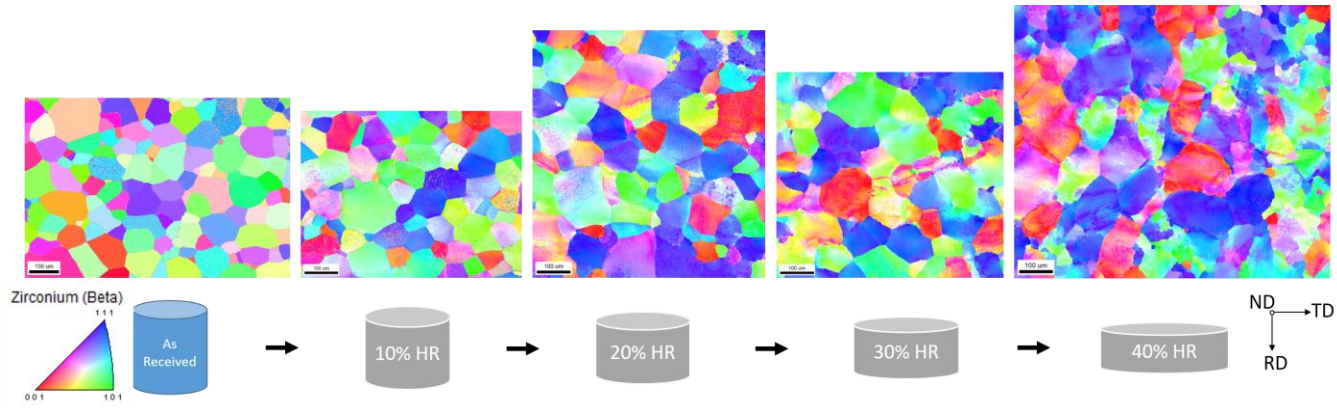

Figure 14: EBSD Inverse pole figure (IPF) map of the experimental sample at each step in the processing path. Colors represent the BCC crystallographic orientation based on the IPF map shown to the right. Scans show only the beta phase. Each scale bar reads 100μm

CHAPTER 5. DISCUSSION

The texture components of interest in this paper are those of hot rolling, cold rolling and recrystallization in BCC alloys. This is largely due to the unconventional processing path of the samples. To review, the samples were hot rolled at 1000°C at 1% increments to each reduction stage with intermittent annealing to 1000°C for 5 minutes. After the 10%, 20%, 30%, and 40% reductions were reached the sample was annealed back to 1000°C for another 5 minutes and quenched in water. Considering that the EBSD and XRD analysis was conducted after the samples annealed and quenched, the results are expected to exhibit recrystallization textures along with rolling components as well. Since recrystallization textures are highly dependent on a sample's initial texture [22, 27, 29], it is of interest to see the overarching effect of the HR + annealing process as reduction is increased.

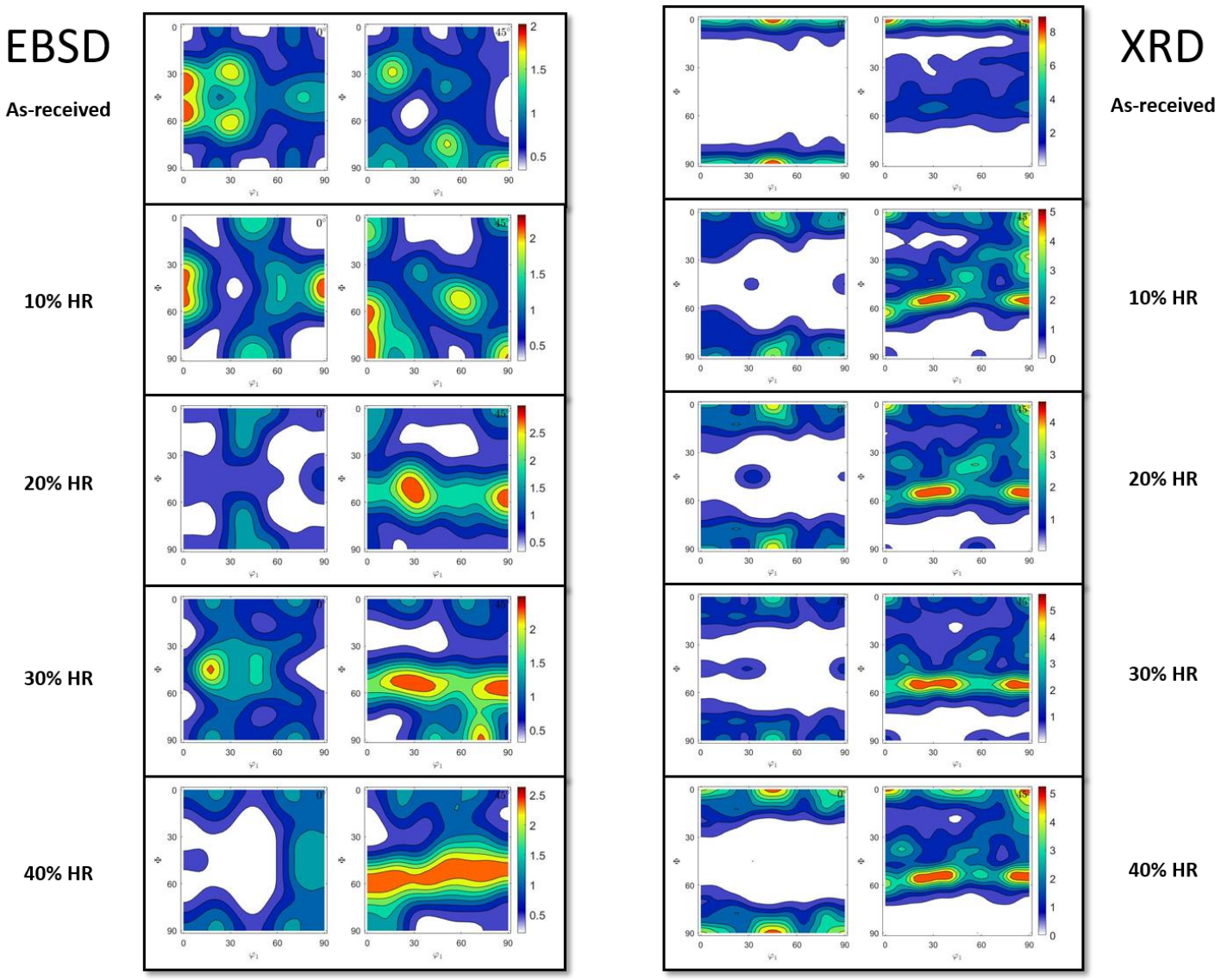

Figure 15: ODF sections, φ_2 =0° and φ_2 =45°, of microtexture data from EBSD on the left and texture data from XRD on the right for each stage of the processing path

5.1 EBSD ODF Analysis

On the left hand side of Figure 15 shows the φ_2 =0° and φ_2 =45° ODF sections acquired by EBSD of the as-received sample and each subsequent height reduction stage in the hot rolling process. The most apparent trend is the formation and intensity homogenization of

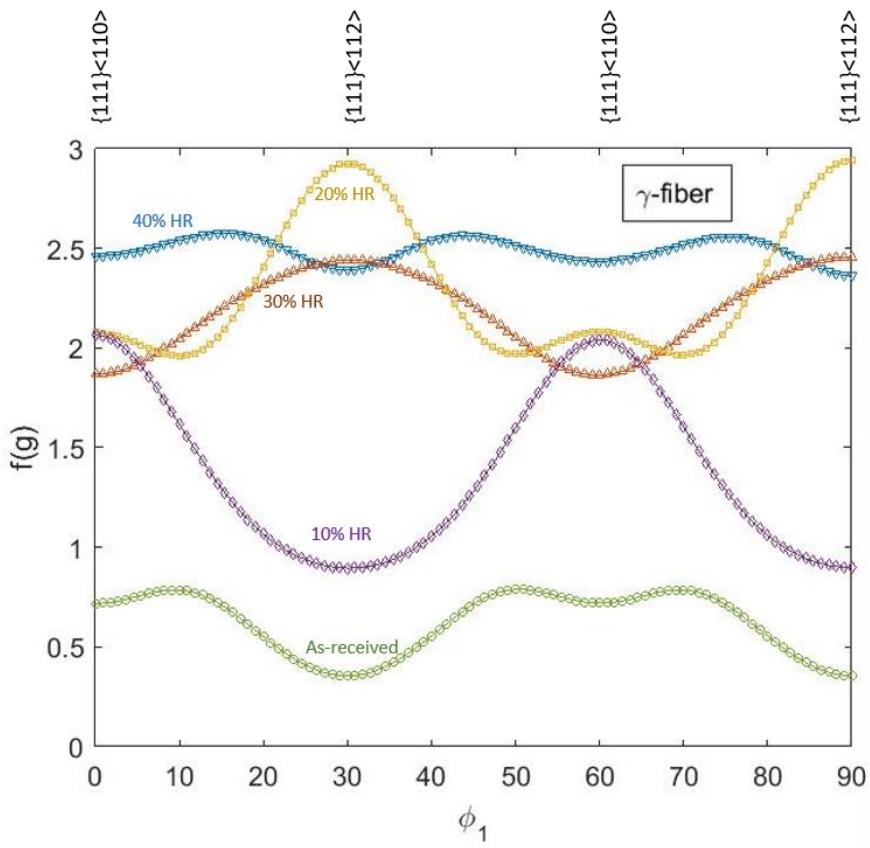

Figure 16: γ-fiber intensity chart corresponding to EBSD ODF data

the γ-fiber with increased reduction. It is also apparent that the α-fiber is either weak or non-existent throughout processing. The as-received texture is absent of any γ-fiber components. The transition from 10% HR to 20% HR shows a slight formation of an α-fiber around the {001}<110> component and an intensity peak along the gamma fiber that moves from {111}<110> in 10% HR to {111}<112> in 20% HR. In the 20% HR and 30% HR, the γ-fiber is dominated by the {111}<112> component but slightly decreases in its intensity overall. In the 40% HR step, a homogeneously occupied γ-fiber is formed with the increase of the {111}<110> component. In the $\phi 2 = 0°$ sections of the ODF the as-received sample shows strong intensities at the {034}<100> and Goss {110}<100> components along the η-fiber. These textures are still present in the 10% HR sample

however a weak R-cube texture is also introduced. In the 20% HR sample the η-fiber components have been eliminated but the R- cube texture is still present. In the 30% HR

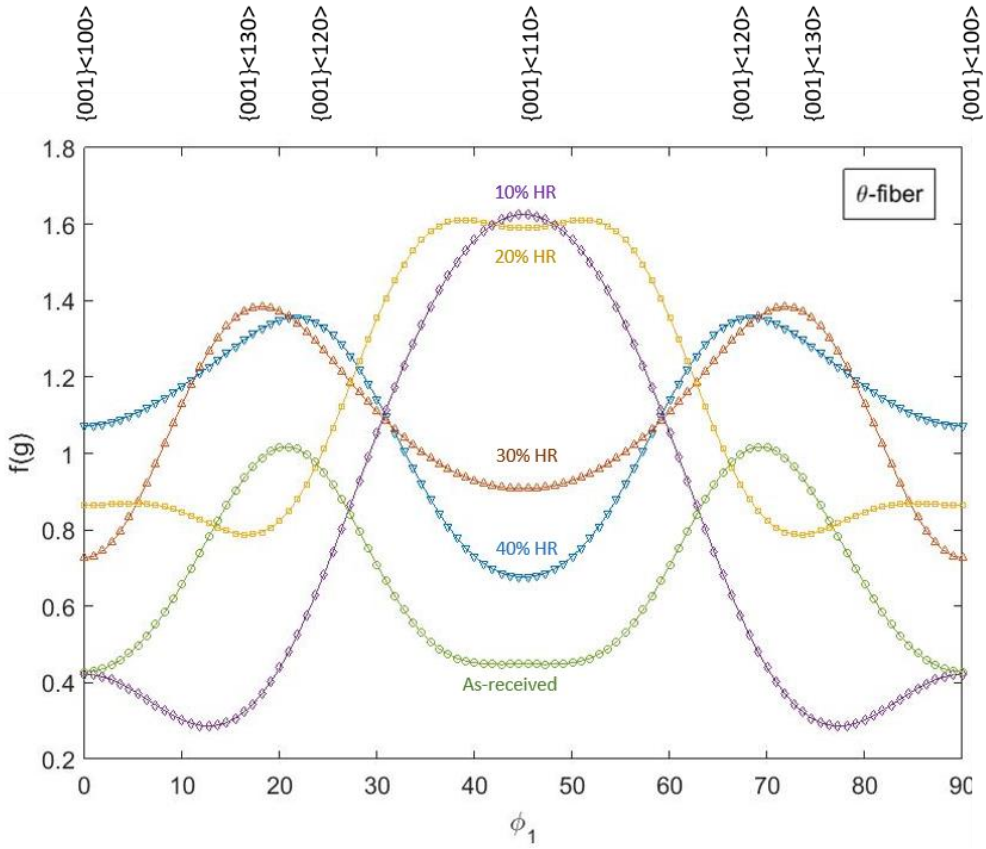

Figure 17: θ-fiber intensity chart corresponding to EBSD ODF data

sample there is a peak intensity at a Brass/Goss component and the weak rotated cube texture has split into the {001}<120> component which remains in the 40% HR sample as well. The evolution of the γ-fiber and θ-fiber can be easily observed in Figure 16 and Figure 17, respectively. The intensities, f(g), indicates "times random" texture and the intensities are plotted along the φ_1 direction. The intensities are weak over all in both fibers which can be attributed to the low reductions the sample has undergone in addition to the multitude of hot-rolling and annealing steps which may have induced dynamic

recrystallization. The latter can also explain the low intensities of the α-fiber at low deformation and lack of the α-fiber at higher deformation.

5.2 XRD ODF Analysis

Figure 15 shows the φ_2 =0° and φ_2 =45° ODF sections acquired by XRD using the (002), (112), (123), and (222) peaks. The intensity graphs in Figure 18 and Figure 19 also help follow the evolution of the θ and γ fibers respectively. The As-received sample shows a strong R-cube texture accompanied with moderately intense components along the θ-

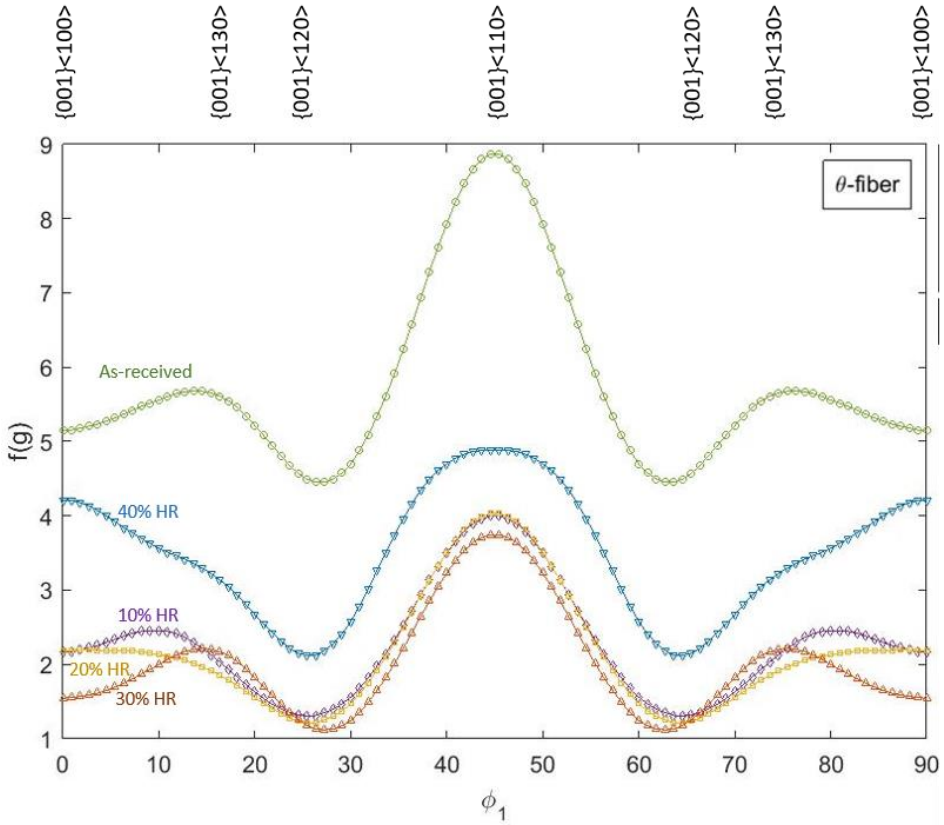

Figure 18: θ-fiber intensity chart corresponding to XRD ODF data

fiber. In addition, there is a weak γ-fiber present with intensities slightly higher at the {111}<112> orientation. The 10% HR and 20% HR textures show significantly less intensity in the θ-fiber and R-cube component but the θ-fiber intensity follows the same

pattern along the φ_1 direction as in the as-received sample. In contrast the γ-fiber in the 10% HR sample is dominating in comparison to the as-received sample, still with the highest peaks at the {111}<112> component. The intensity of the γ-fiber in the 20% HR sample is just slightly less than that of the 10% HR at the {111}<112> component but slightly higher at the {111}<110> component, though the {111}<112> still dominates the texture. In the 30% HR sample, the intensity of the γ-fiber is the highest however there is a shift in the peak intensity to the {111}<123> orientation. This shift remains in the 40% HR sample but has a slightly lower intensity γ-fiber. The 30% HR texture shows the least intensity in the R-cube component and θ-fiber. This intensity jumps at the 40% HR sample

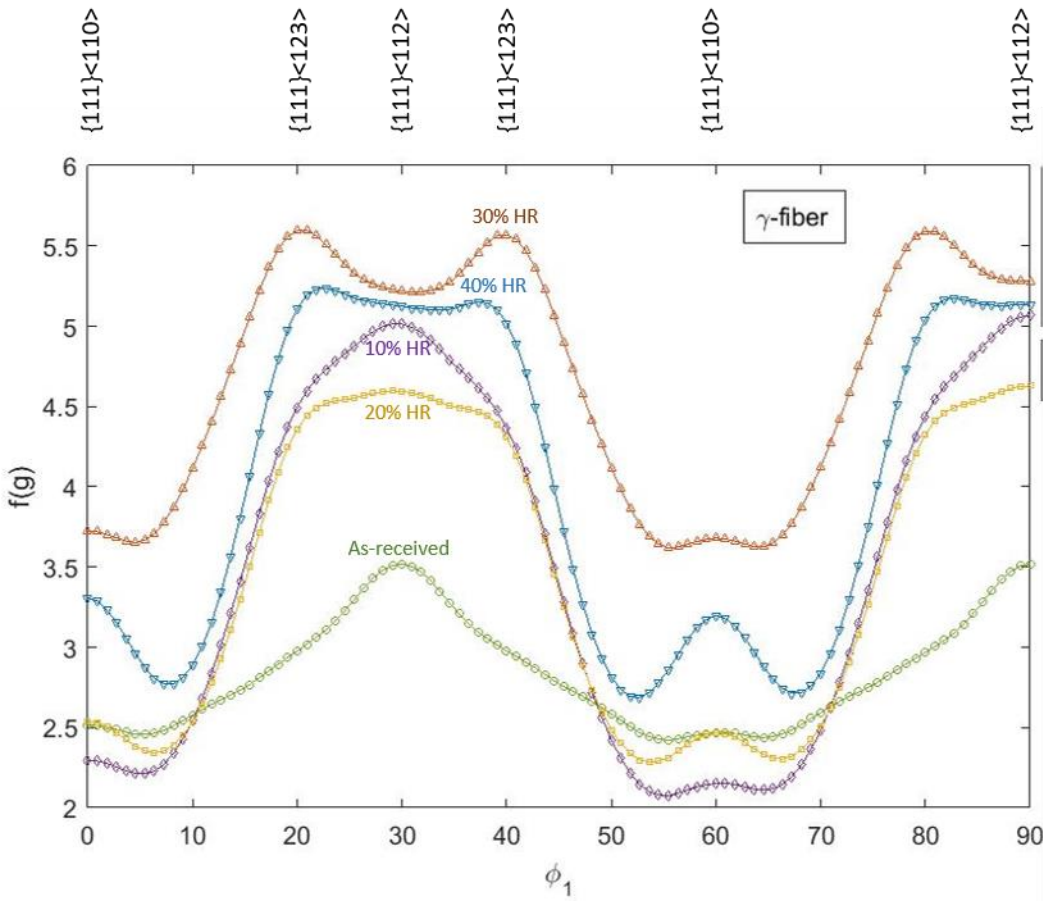

Figure 19: γ-fiber intensity chart corresponding to XRD ODF data

showing a larger R-cube and additional cube component but this intensity is still significantly lower than the as-received texture.

In Figure 18 it is apparent that the highly textured as-received sample leaves a lasting effect on the rolling and recrystallization textures with increased reduction. Though less in intensity, the dominant texture in the θ-fiber remains rotated cube throughout processing. This texture may be the result of the manufacturing of the as-received rod. The drop-casting method may have induced the growth of columnar grains while solidifying. In cubic materials, the columnar grains grow in the <001> direction which explains the strong θ-fiber. In Figure 19, the γ-fiber increases overall as reduction increases. The periodic sharp increase in the {111}<112> component followed by the slight decrease in intensity may be due to the influence of the preceding texture on the subsequent texture. With increased reduction the {111}<110> orientation first decreases in intensity and then gradually increases in intensity following the pattern of the {111}<112> component.

5.3 Analysis of Texture Evolution

Analysis of the EBSD and XRD ODFs brings to light certain apparent trends in the θ-fiber and γ-fiber evolution which can be justified by the specifics of the processing path. As well, the lack of the α-fiber can be explained by understanding the nature of hot-rolling and annealing processes in BCC materials. Initial texture also plays a role in texture development which is illustrated in both EBSD and XRD data through the progression of the process path. Finally, some information about hot-rolling deformation texture can be revealed by analyzing the subsequent annealing texture.

The EBSD microtexture data was largely characterized by a strengthening γ-fiber with increased deformation and a weak or lacking α-fiber. The XRD texture data showed a strengthening γ-fiber which had not reached homogeneous intensity across the fiber and also a weak α-fiber. It is important to note that this data was acquired after the HR + annealing steps at each stage in processing meaning that both rolling and recrystallization textures would be present in each of the ODF sections. One explanation for this texture evolution behavior could be explained by the oriented growth theory of recrystallization. This theory states that the final recrystallization texture of a material will depend on the growth rate of initial nulei formed during the annealing process. This growth rate would be determined by the orientation relationship between the nuclei and surrounding matrix which would allow certain nuclei grain boundaries to have a higher mobility than others. This is theory was preceded by the oriented nucleation theory which stated that the final recrystallization texture would depend on the orientation of the initially formed nuclei. This theory suggested that the orientation that dominated the initial nuclei would dominate the final recrystallization texture. Emren et al. [29] observed the oriented growth phenomenon in deep drawn steels which were cold rolled and subsequently annealed. In these BCC steels, annealing strengthened the γ-fiber particularly at the {111}<112> components at the expense of the {112}<110> α-fiber component. The mechanism is illustrated in Figure 20. Deformation is known to develop the α-fiber and therefore prior to annealing there are ample locations in the sample with the {112}<110> orientation. The {111}<112> γ-fiber nuclei have a favorable orientation relationship with the {112}<110> deformed matrix which allows for a high growth rate of the γ-fiber component. Though the {111}<110> γ-fiber nuclei have a favorable matrix component located at $\phi = 20°$ on

the α-fiber, this component is generally less densely populated in the deformed sample. During the recrystallization process, the {001}<110> component is unfavorable for

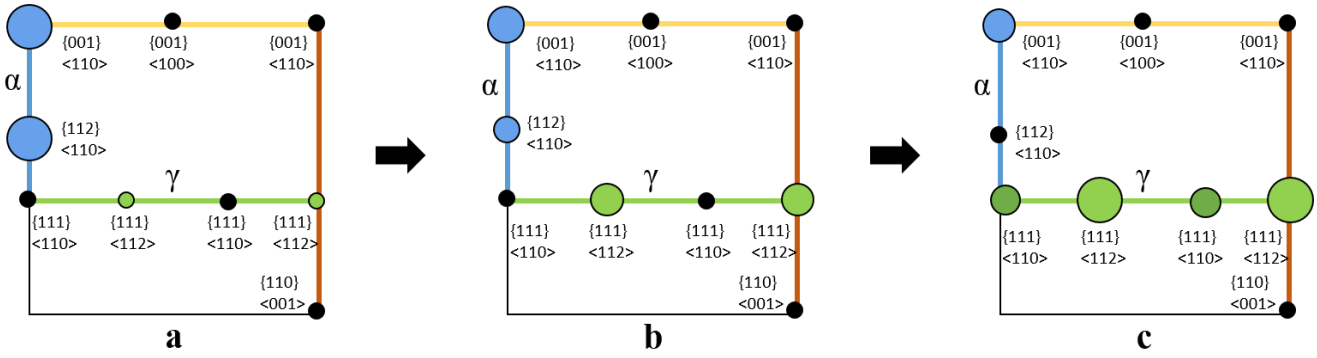

Figure 20: Schematic of growth of γ-fiber upon annealing due to oriented growth in BCC metals and alloy. The figure shows the progression of recrystallization where a) shows a φ_2 = 45° section of cold rolled BCC material, b) shows a φ_2 = 45° section of material after initial stages of recrystallization, and c) shows a φ_2 = 45° section of material after later stages of recrystallization

nucleation and growth of the λ-fiber nuclei and therefore this component consistently outlasts other α-fiber components. Both EBSD and XRD ODFs show evidence of the {001}<110> component in the α-fiber and no other components with comparable intensity. However the growth of the γ-fiber is strong which suggests that during hot-rolling steps the α-fiber may have developed and become consumed during annealing.

Apart from the oriented growth theory, there is another trend in the EBSD data which suggests that at higher rolling + annealing stages, the sample may be undergoing secondary recrystallization. At 10% and 20% HR the sample shows some R-cube texture which then splits into the {001}<120> component in the 30% and 40% HR samples. The intensity of these components is significantly weaker than the γ-fiber components and the {001}<120> component is only observed in the micro-texture from EBSD and therefore it is believed that secondary recrystallization is occurring at a very small degree at localized regions in

the sample. Secondary recrystallization in various BCC metals and alloys is described in detail by Dillamore et al. [27]. It is said to occur when primary grain growth has been restricted by either a weakly textured primary matrix or by inclusions along grain boundaries. Though only β-phase evolution was monitored in this work, the sample was populated with α-precipitates both within grains and along grain boundaries which may have limited grain growth during annealing steps. Secondary recrystallization occurs when there is irregular grain growth of certain orientations. Dillamore et al. [27] found that the frequently obtained secondary recrystallization textures included Goss and cube textures. In recent studies on electrical or magnetic steels [25, 31] the {001}<120> component along the θ-fiber was reported to from after prolonged recrystallization or secondary recrystallization. One study by Siqueira et al. [25] found that the R-cube texture formed by cold rolling Nb-containing ferritic stainless steel actually split into the {001}<120> component upon secondary annealing. This is similar to the ESBD results in this work but at a much lower intensity.

Another observation that needs to be addressed due to the nature of the processing procedure is the effect of initial texture on subsequent texture. The standard texture evolution procedure involves collecting initial texture data followed by rolling texture data, and finally annealing texture data. Instead in this work, the texture data is collected of the initial sample and after the annealing step following each rolling reduction. Though the process stays the same at each stage in the process path, the starting texture is different and this means that the subsequent texture formation due to processing would be affected. This can be seen in the XRD texture intensity plot for the γ-fiber. Although there is a general increase in the strength of the fiber, there is a fluctuation in the direction of growth of the

{111}<112> component with each increase in deformation. This can be due to the growth of certain components into the matrix of the sample that no longer allow for preferred orientation growth of the expected orientations. Lee et al. [32] investigated the effect of initial texture in an interstitial free steel by performing a 1st and 2nd cold rolling + annealing treatment and collecting texture data at all 4 stages of processing. After the 1st cold rolling and annealing the results were as expected. However due to the large amount of {111}<112> component present in the sample at this point further nucleation and growth of the {111}<112> component during the 2nd annealing would have been unfavorable and therefore the {111}<110> component had a larger growth rate and dominated the texture. A similar effect can be occurring the Zr-Nb sample to cause the fluctuation of the {111]<112> intensity. In addition, the strongly textured R-cube component in the as-received sample seems to also affect subsequent texture formation in the XRD data. The distribution of the θ-fiber components is overall consistent throughout processing apart from the drop in intensity. This strong initial texture may be affected by the small rolling reductions but not enough to disrupt the pattern of the θ-fiber until further deformation as can be seen with the increase in the cube texture at 40% HR.

CHAPTER 6. CONCLUSION

In nuclear forensics, a deeper analysis of a material's microstructure can reveal key signatures that connect the microstructure to its process path and ultimately its origin. Texture analysis has long been the tool that material scientists use for exactly this purpose. This work followed the texture and microtexture evolution of drop-casted BCC Zr-18wt%Nb alloy as it underwent hot-rolling and intermittent annealing. The results obtained using XRD and EBSD were compared with various BCC metals and alloys.

In general, rolling and recrystallization textures of BCC materials remain similar despite the material composition. A less studied phenomenon is the evolution of BCC texture as it undergoes an unconventional process of intermittent hot-rolling and annealing. The effects of rolling and recrystallization remain in the microstructures in this work however the evolution of texture over repeated hot-rolling and annealing to various degrees of reduction have revealed new patterns in the texture that have not been comprehensively studied. Upon analysis of the texture and microtexture data, the following conclusions can be made about the texture evolution.

First, the EBSD results are consistent in illustrating the initial growth of {111}<112> component at low reductions and increasing intensity of {111}<110> at higher deformation. This is concluded by treating the 10%HR sample as an outlier because it shows a dominant {111}<110> texture along the γ-fiber though the deformation stage is low. This can be attributed to the local inhomogeneities in the sample surface.

Also, EBSD and XRD results show evidence to support the oriented growth theory for {111}<112> nuclei in a {112}<110> matrix. This is supported by the strength of the {111}<112> component along the γ-fiber and absence of the {112}<110> component altogether.

Secondary recrystallization is believed to be occurring later in the rolling process which would explain the {001}<120> component formation in the 30% and 40% HR samples. This is only observed in the EBSD data at low intensities which suggests that the surface microtexture differs from the texture of the sample as a whole.

XRD data shows fluctuations in the direction of growth of the γ-fiber intensity indicating that preceding texture may determine the evolution of texture after the next processing step. XRD data shows that original sample is heavily textured with R-cube and the pattern of the θ-fiber has remained relatively the same apart from changes in intensity. These both illustrate that initial texture can largely affect the subsequent texture.

Finally, the α-fiber is primarily strengthened during deformation. The lack of evidence of a strong α-fiber in the ODF data does not necessarily mean that hot-deformation did not produce a strong α-fiber. Rather it is likely to have been consumed and eliminated due to dynamic recrystallization and annealing steps as the process progressed.

CHAPTER 7. FUTURE WORK

The present work has arrived at various conclusions based on the performed experiments using optical microscopy, XRD, and EBSD. This analysis has prompted a number of techniques and experiments which can facilitate the processing and the collection of texture data for future texture evolution studies. This chapter will discuss the recommended experiments to supplement this work and the future implications of this study will be explored in regards to inverse process path modeling and nuclear forensics.

The processing in this work ceased with 40% rolling reduction, however deformation studies in BCC materials indicate dramatic texture changes can occur beyond 70% reduction [29], and therefore further reduction using the unconventional processing of this work would be insightful. The hot-rolling process is also known to induce dynamic recrystallization in the sample which can become indistinguishable from recrystallization texture due to annealing. For this reason it would be beneficial to perform an equivalent texture evolution study with cold-rolling and intermittent annealing for comparison.

In regards to the texture data collection, there are three avenues of future work that can further clarify the mechanism of texture evolution. The first requires the characterization of the sample after the desired rolling reduction has been achieved before the next annealing step. Collecting purely deformation texture data could provide insight into deformation texture that cannot be predicted by subsequent annealing data. In addition, EBSD microtexture data in this work was collected near the center of the sample on the normal surface at each stage in the processing path. Using micro-indentation markers to isolate a particular area on the sample would allow for consistent and exact micro-texture

evolution measurements at each rolling step. Furthermore, EBSD can elucidate the exact mechanism of recrystallization due to annealing through the use of orientation maps overlaid on top of the EBSD scan. This would provide a physical representation of orientation density in a sample and help illustrate mechanisms such as grain growth and secondary recrystallization.

This work also encountered the precipitation of the hcp α-phase whose texture data was unable to be extracted from the performed experiments. One method of exploring the β to α transformation texture would involve prolonged aging of a β-quenched sample. Growth of the α precipitates would facilitate with both EBSD scans and XRD peak analysis. The metastable ω-phase was also briefly discussed in the introduction. This phase precipitates athermally upon quenching to form nano-precipitates which are essentially undetectable with EBSD and XRD and therefore transmission electron microscopy (TEM) could provide a full analysis of phase distribution throughout the processing path.

Upon completion the experimental study of one variation of thermo-mechanical processing on monotectoid BCC Zr-Nb, both micro-texture and texture and grain size data have been acquired and analyzed for multiple stages in processing. Ultimately, the work presented in this thesis serves to provide experimental validation for an inverse process path model. This model would input this microstructural information and by analysing the texture changes from step to step in the processing path, a processing parameter could be attained. Calculating a processing parameter would allow one to model an initial microstructure from a given final microstructure.

In regards to nuclear forensics, the purpose of texture data collection is to generate a microstructural hull. A microstructural hull can be visualized as a 3D space which encompasses every possible material texture that can be formed through a number of processing techniques. Each point in the hull represents a texture and processing paths are represented as streamlines that connect textures obtained through various degrees of processing. With a library of interconnected points and streamlines populating the microstructural hull, a forensics expert could select the optimal processing path that led to a given final microstructure. This path could be predicted based on the capabilities of different processing facilities which contribute certain microstructural signatures, or it could pertain to efficiency and probability of a particular processing path.

REFERENCES

1. *Chapter 1 - Phases and Crystal Structures*, in *Pergamon Materials Series*, S. Banerjee and P. Mukhopadhyay, Editors. 2007, Pergamon. p. 1-86.

2. Srivastava, D., et al., *Evolution of Microstructure, Microtexture and Texture in Dilute Zirconium Based Structural Components of Pressurised Heavy Water Reactors.* 2009(43512): p. 401-409.

3. Nikulina, A.V., *Zirconium-Niobium Alloys for Core Elements of Pressurized Water Reactors.* Metal Science & Heat Treatment, 2003. **45**(7/8): p. 287-292.

4. Nomura, N., et al., *Effects of Phase Constitution of Zr-Nb Alloys on Their Magnetic Susceptibilities.* MATERIALS TRANSACTIONS, 2009. **50**(10): p. 2466-2472.

5. Zhou, F.Y., et al., *Microstructure, corrosion behavior and cytotoxicity of Zr–Nb alloys for biomedical application.* Materials Science and Engineering: C, 2012. **32**(4): p. 851-857.

6. Abriata, J.P. and J.C. Bolcich, *The Nb−Zr (Niobium−Zirconium) system.* Journal of Phase Equilibria, 1982. **3**(1): p. 34-44.

7. Choo, K.N., et al., *Effect of composition and heat treatment on the microstructure and corrosion behavior of Zr ‧ Nb alloys.* Journal of Nuclear Materials, 1994. **209**(3): p. 226-235.

8. Jeong, Y.H., K.O. Lee, and H.G. Kim, *Correlation between microstructure and corrosion behavior of Zr–Nb binary alloy.* Journal of Nuclear Materials, 2002. **302**(1): p. 9-19.

9. Zaluzec, N.J., *Analytical electron microscope study of the omega phase transformation in a zirconium--niobium alloy*. 1979, ; Oak Ridge National Lab., TN (USA). p. Medium: ED; Size: Pages: 334.

10. Kondo, R., et al., *Effect of cold rolling on the magnetic susceptibility of Zr–14Nb alloy.* Acta Biomaterialia, 2013. **9**(3): p. 5795-5801.

11. Devaraj, A., et al., *A low-cost hierarchical nanostructured beta-titanium alloy with high strength.* Nature Communications, 2016. **7**: p. 11176.

12. Hehemann, R.F., *Transformations in zirconlum-niobium alloys.* Canadian Metallurgical Quarterly, 1972. **11**(1): p. 201-211.

13. Raabe, D., *Simulation of rolling textures of b.c.c. metals considering grain interactions and crystallographic slip on {110}, {112} and {123} planes.* Materials Science and Engineering: A, 1995. **197**(1): p. 31-37.

14. Hu, H., *Texture of Metals.* Texture, 1974. **1**(4): p. 233-258.

15. Nishimura, K., S. Hanada, and O. Izumi, *Tensile properties and plastic deformation modes ofβ Zr-Nb alloys.* Journal of Materials Science, 1990. **25**(1): p. 384-390.

16. Brown, D., et al., *Aging and deformation of uranium-niobium alloys*. Vol. 30. 2006. 79-83.

17. Koike, J., et al., *The Nb-U (Niobium-Uranium) system.* Journal of Phase Equilibria, 1998. **19**(3): p. 253-260.

18. Sagaradze, V.V., et al., *Structural heredity in the U-6Nb alloy and conditions for its elimination.* The Physics of Metals and Metallography, 2013. **114**(4): p. 299-307.

19. Bunge, H.J., *2 - Orientation of Individual Crystallites*, in *Texture Analysis in Materials Science*. 1982, Butterworth-Heinemann. p. 3-41.

20. *Electron Backscatter Diffraction in Materials Science*. 2 ed. 2009: Springer US. XXII, 403.

21. Bunge, H.J., *3 - Orientation Distributions*, in *Texture Analysis in Materials Science*. 1982, Butterworth-Heinemann. p. 42-46.

22. Hölscher, M., D. Raabe, and K. Lücke, *Rolling and recrystallization textures of bcc steels.* Steel Research, 1991. **62**(12): p. 567-575.

23. Raabe, D., *Overview on Basic Types of Hot Rolling Textures of Steels.* steel research international, 2003. **74**(5): p. 327-337.

24. Verbeken, K., et al., *Effect of Hot and Cold Rolling on Grain Size and Texture in Fe-2.4wt%Si Strips*. Vol. 44. 2008. 3820-3823.

25. Siqueira, R., H. Sandim, and T. Oliveira, *Texture evolution in Nb-containing ferritic stainless steels during secondary recrystallization*. Vol. 497. 2008. 216-223.

26. Raabe, D., *Rolling and annealing textures of a ferritic stainless steel with 11 mass%Cr content.* Textures of Materials, 1996: p. 330-335.

27. Dillamore, I.L. and W.T. Roberts, *PREFERRED ORIENTATION IN WROUGHT AND ANNEALED METALS.* Metallurgical Reviews, 1965. **10**(1): p. 271-380.

28. Raabe, D. and K. Lücke, *Annealing textures of BCC metals.* Scripta Metallurgica et Materialia, 1992. **27**(11): p. 1533-1538.

29. Emren, F., U. Vonschlippenbach, and K. Lucke, *Investigation of the development of the recrystallization textures in deep drawing steels by ODF analysis*. Vol. 34. 1986. 2105-2117.

30. *ASTM E112-13 Standard Test Methods for Determining Average Grain Size*. 2013: West Conshohocken, PA.

31. Liu, J.L., et al., *Development of strong {001}〈210〉 texture and magnetic properties in Fe–6.5wt.%Si thin sheet produced by rolling method.* Journal of Applied Physics, 2011. **109**(7): p. 07A326.

32. Young Lee, K., G. Sung Kim, and L. Kestens, *Effect of Initial Texture on the Evolution of Texture and Stored Energy during Recrystallization of Interstitial Free Steel*. Vol. 495-497. 2005. 357-362.